Advanced Steel Construction – Vol. 18 No. 1 (2022) 517–527
DOI:10.18057/IJASC.2022.18.1.10

LOW-CYCLE FATIGUE PROPERTIES OF AUSTENITIC STAINLESS STEEL S30408 UNDER LARGE PLASTIC STRAIN AMPLITUDE

Lei Chen [1, 2], Dong-Sheng Wang [1, 2, *], Fan Shi [1, 2] and Zhi-Guo Sun [3]

[1] *School of Civil and Transportation Engineering, Hebei University of Technology, Tianjin 300401, China*
[2] *Civil Engineering Technology Research Center of Hebei Province, Tianjin 300401, China*
[3] *Key Laboratory of Building Collapse Mechanism and Disaster Prevention, Institute of Disaster Prevention, China Earthquake Administration, Beijing 101601, China*
** (Corresponding author: E-mail: dswang@hebut.edu.cn)*

ABSTRACT

The application of stainless steel materials in civil structures for seismic protection lies in its low-cycle fatigue characteristic. However, the data of existing research are mainly based on the low-cycle fatigue in small strain amplitudes. To this end, we perform low-cycle fatigue testing of Austenitic stainless steel S30408, which has low yield point and good elongation performance, under the cyclic load with a maximum strain amplitude reaching up to 5%, to fill the gap. The stress-strain response characteristics of the stainless steel material under the cyclic load are analyzed; then, the parameters of the strain-fatigue life relationship and the cyclic-plastic constitutive model used for FEA simulation are extracted. Results show that the stainless steel's stress-strain curve is nonlinear without a yield plateau, thus presenting a high strength yield ratio and ductility. The hysteresis loops of the material are plump with a shuttle shape and are symmetric to the origin, indicating a fine energy dissipation capacity. The skeleton curve under cyclic loading with cyclic hardening can be significantly reflected by the Ramberg-Osgood model, which is affected by the strain amplitude and loading history; it is also different from the monotonic tensile skeleton curve. The strain-fatigue life curve fitted by the Baqusin-Manson-Coffin model can predict the materials' fatigue life under different strain amplitudes. The mixed hardening model, including isotropic and kinematic hardening, based on the Chaboche model, is able to simulate the cyclic stress-strain relationship. Further, its parameters can provide basic data information for the seismic design of civil structures when Austenitic stainless steel S30408 is used.

ARTICLE HISTORY

Received: 28 April 2021
Revised: 30 May 2021
Accepted: 22 July 2021

KEYWORDS

Austenitic stainless steel;
Low-cycle fatigue;
Cyclic stress-strain response;
Strain-fatigue life;
Mixed hardening;
Chaboche model

1. Introduction

The advantages of stainless steel materials, such as strong corrosion resistance, good ductility, and easy processing, have made it not only useful in the tableware, sculpture, and automobile fields but also in civil structures like bridges, ports, and underground projects [1, 2]. For example, 8,200 tons of stainless steel bars were applied to construct pile caps, tower seats, and piers for the Hong Kong-Zhuhai-Macao Bridge [3]. Stainless steel can also significantly reduce costs associated with durability maintenance and improve economic efficiency over a structure's entire life cycle.

The capability design criterion in the seismic design of structures allows designers to make full use of energy dissipation components or regions to reduce seismic responses by employing the elastoplastic hysteretic properties of materials with a rational design [4]. Under seismic loading, structures usually need to withstand short-term and huge reciprocating forces. Structural members, especially those acting as dissipation components [5], experience several large displacement cyclic loadings, which are manifested by low-cycle fatigue (LCF) with large strains at the material level. Therefore, it acts as a basis in which to investigate the stainless steel material's low-cycle fatigue performance for application in structural seismic design.

In previous studies, stainless steel exhibited an obvious nonlinear stress-strain relationship, and it is different from that of typical plain steel. Arrayago et al. [6] compiled 600 monotonic tensile tests for ferritic, austenitic, and duplex stainless steels, including grades and rolling directions of a variety of materials. They then proposed amendments for the prediction of model constitutive parameters. Under cyclic loading, the hysteresis loop of stainless steel material is plump and stable, indicating a fine hysteresis behavior; further, the cyclic skeleton curve is different from the monotonic tensile curve tension, showing an obvious strain hardening phenomenon [7-9]. In addition, it has been revealed that the cyclic hardening characteristics are greatly affected by plastic strain amplitude as well as the loading process. Further, the history and amplitude of the first load before the next cycle can influence the cyclic stress-strain curve [10, 11]. The number of times the test piece can withstand cyclic loading, i.e., the fatigue life of coupons, is a factor to be considered in its application. Julie et al. analyzed the strain-fatigue life relationship of stainless steel materials with strain below 2.0% and introduced a prediction formula for fatigue life [12, 13]. Accurate material constitutive models and parameters are the foundation for structural design and seismic performance analysis of structures. Stainless steel presents mixed hardening characteristics when reciprocated loading is applied [14]. In addition, the Chaboche constitutive model is well used currently, and its applicability have been studied by some researchers [15, 16].

Austenitic and Duplex stainless steel, which have different low-cycle fatigue characteristics, are mainly used in structures. Austenitic stainless steel with low yield point and good elongation performance has the advantage of corrosion-resistance and characteristic of low yield point steel [17]. For a high production capacity and widely used austenitic stainless steel, S30408, has good cold working performance, high toughness and good high-temperature resistance. In general corrosion, it can satisfy the requirements of corrosion resistance [18]. And the price of S30408 is lower, which represents that it is more conducive to the use and promotion of structures. It is an optimal material choice under the consideration of reliable durability performance and cost economy. In structural seismic design, it is frequently used in energy-dissipating devices, as the core of a buckling-restrained brace (BRB), where its design interface mostly consists of plate specimens [19, 20]. These devices need to withstand large plastic deformations under seismic loads [21]. However, previous studies on materials, to the best of our knowledge, have mostly focused on small strain high- or low-cycle fatigue of round bars, which cannot satisfy the needs of seismic design. Fewer studies about cyclic loading and fatigue life of plate specimens had been reported.

Therefore, three types of Austenitic stainless steel S30408 specimens, including plates and bars, are considered in this study. Three loading systems, consisting of monotonic tensile, constant, and variable strain amplitude cyclic loading with the strain amplitude reaching up to 5%, are carried out to analyze the material's characteristics. The key mechanical indexes and constitutive parameters of the monotonic model are determined through a uniaxial tensile test. We adopt the Ramberg-Osgood model to depict the cyclic hardening performance and also use it to fit the cyclic skeleton curves for obtaining the cyclic hardening parameters. The Baqusin-Manson-Coffin model is utilized to fit the strain-fatigue life equation under constant strain amplitude cyclic loading. For the variable strain amplitude cyclic loading, the Chaboche constitutive model adopted from Abaqus is used to derive the mixed hardening parameters and simulate the cyclic stress-strain relationship. The test pieces used in this test were all from the same batch.

2. Experimental details

2.1. Material and coupon specifications

Austenitic stainless steel S30408, which is being increasingly applied in buildings, bridges, energy dissipation components, and so forth, was tested in the present study. The chemical components of the stainless steel material are tabulated in Table 1. The specimens were fabricated from the same batch of material along the same orientation into flat and round coupons, including a reduced effective section area in a central region, to constrain the location of the

fracture and a smaller length of the parallel section to avoid buckling [7, 22]. Three kinds of test coupons with different specifications and sizes, defined as LF, SF, and CF, were manufactured based on the Chinese National Standard GB/T26077 [25], and their cross-section forms are a rectangle, square, and circle, respectively, as presented in Fig. 1. The length and thickness of the parallel section for LF coupons is 40 mm and 8 mm, respectively, leading to a sectional length-to-width ratio of 5. To avoid compressive buckling instability in the LF specimen, a buckling-restrained device was designed and then given a heat treatment to ensure hardness. Sandpaper was used to polish the section to reduce the roughness; grease and boron nitride powder were applied on the splint to reduce friction between the test piece and the buckling-restrained device. The SF coupons have a section width of 16 mm with a parallel segment length of 25 mm. And the CF coupons have a section diameter of 20 mm with a parallel segment length of 25 mm.

To accurately apply displacement and prevent the extensometer from sliding under large strain loading, two notches with the width and depth all equal to 0.2 mm were carved along the width direction of the coupons, as shown in Fig. 1. Their locations are at the tip of the extensometer fixed on the specimen. Another, coupon LF´, had the same size as the LF specimen, but for comparison no notch was carved.

Table 1
Chemical components of austenitic S30408

Chemicals	C	Si	Mn	P	S	Cr	Ni	N
Percentage (%)	0.04	0.37	1.10	0.032	0.001	18.17	8.03	0.05

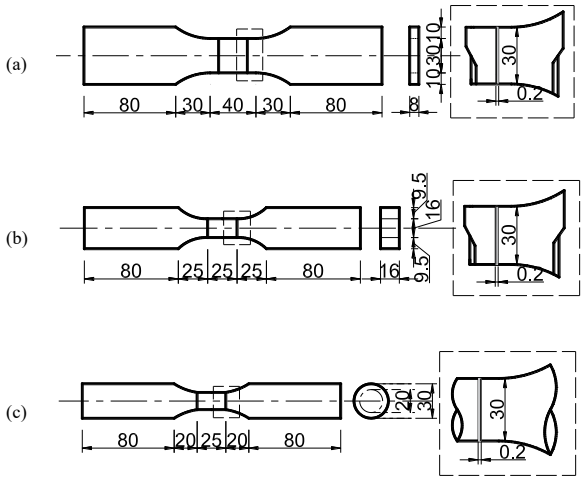

Fig. 1 Geometry of the specimens (units: mm): (a) LF; (b) SF; and (c) CF

2.2. Test setting and loading codes

Axially loaded tests were conducted for the monotonic tensile test to determine the basic mechanical parameters and for the low-cycle fatigue loading test to calibrate the hardening model parameters; then, the strain-fatigue life relationships were established. It should be noted that a larger length-to-diameter (width) ratio is necessary for the standard tensile test piece, according to the Chinese National Standard GB/T 228.1-2010 [23]. Some related literature revealed that the difference in monotonic tensile curves between the standard and reduced length-to-diameter is negligible in cases of small strain [24]. As a result, test specimens LF, SF, and CF with reduced length-to-diameter (width) were used for the monotonic tensile test. The accuracy can be guaranteed within the scope of engineering applications. Nine coupons were subjected to the monotonic tensile test. For each specimen specification, three coupons were performed to calculate the average value of the engineering stress-strain response.

In addition, a total of 88 coupons were performed for the cyclic loading test with two loading patterns, i.e., the constant and the variable strain amplitude loading systems. The constant strain amplitude cyclic loading includes 10 loading protocols, where the strain amplitude ranged from ±0.5% to ±5% with strain ratios R_ε equal to -1, as shown in Table 2. In general, three coupons were tested for obtaining the mean value under each constant amplitude scenario. The variable strain amplitude cyclic loading consists of multiple loading protocols, i.e., cyclic ascend and cyclic descend, to investigate stainless steel's hysteresis characteristics, as shown in Fig. 2.

Table 2
Constant amplitude cyclic loading system

Amplitude(%)	0.5	0.75	1.0	1.25	1.5	2.0	2.5	3.0	4.0	5.0
Label	L1	L2	L3	L4	L5	L6	L7	L8	L9	L10

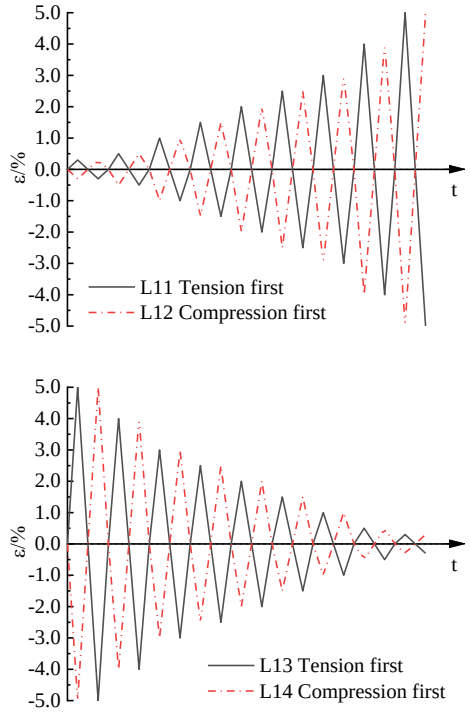

Fig. 2 Variable amplitude cyclic loading system

An MTS 793 system that can apply tension and compression loads was used to conduct monotonic tensile and cyclic loading tests, as presented in Fig. 3. The test coupons were gripped by hydraulic jaws. The monotonic tensile test coupons were executed by using an axial actuator with a loading frequency equal to 2 mm/min under displacement-control according to the Chinese National Standard GB/T228 [23]. Tests of cyclic loading were performed under nominal strain-control of the parallel segment measured by the extensometer, according to the Chinese National Standard GB/T26077 [25]. The extensometer's gauge length was 25 mm with a measuring range equal to ±20% in tension and compression. A triangular waveform loading history was adopted, and the loading frequency was set as 0.02 Hz, through which a slow strain rate can be maintained to reduce instability and heat produced in the loading process. The sampling frequency is 32 Hz. Specimens were marked before applying the load in order to measure the elongation after a fracture. All test data and input information were recorded by the MTS data acquisition system. The experimental device diagrams of the three different specifications and sizes of test specimens are shown in Fig. 4.

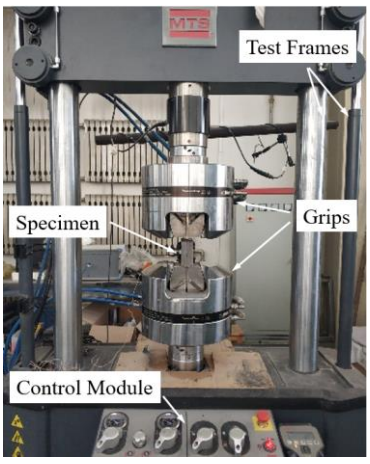

Fig. 3 Loading system with hydraulic grips (MTS793)

(a)

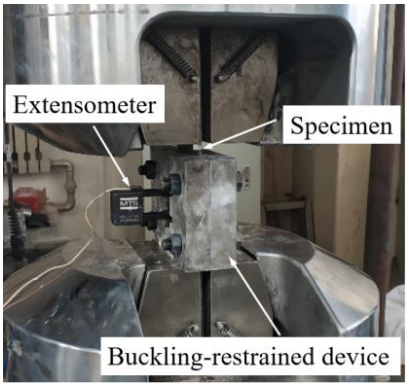

(b)

(c)

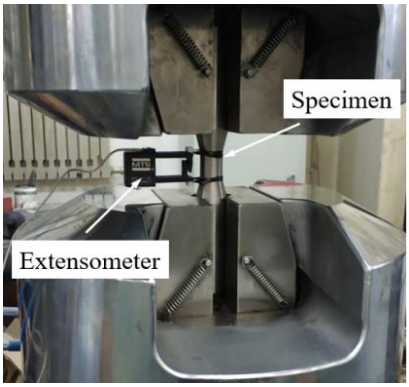

Fig. 4 Cyclic axial test setup: (a) LF; (b) SF; (c) CF

3. Experimental results and discussion

3.1. Results of monotonic experiments

Specimens of different sizes, LF-M1-3, CF-M1-3, and SF-M1-3 (where M represents the monotonic tensile test, and the numbers 1 to 3 indicate the specimen serial number), were subjected to the monotonic tensile loading until they fractured. Table 3 shows the basic mechanical parameters obtained for Austenitic stainless steel S30408. The experiment data reveals that the material has a larger strength-yield ratio of nearly 2.5, which indicates higher safety redundancy for seismic design and higher strain hardening compared with carbon steel. The elongation measured after fracture exceeded 50%, thus demonstrating better ductility and strong plastic deformation ability than the carbon steel. This result is consistent with the result of previous studies on the characteristics of the stainless steel materials [26, 27]. The test data for the LF and CF specimens are not much different from each other in strain, stress, and Young's modulus. The stress of SF was different from the other two specimens, however; the reason for this phenomenon may be that the mechanical performance of the test specimens was affected by temperature during the laser cutting process on account of thickness. When there was a small width-to-thickness ratio, a measurement deviation in the test data would be caused.

Table 3

Mechanical parameters under monotonic tensile loading

Specimen	E/GPa	$\sigma_{0.01}$/MPa	$\sigma_{0.2}$/MPa	$\sigma_{1.0}$/MPa	$\sigma_{2.0}$/MPa	σ_u/MPa	$\varepsilon_{0.2}$/(%)	$\varepsilon_{2.0}$/(%)	ε_u/(%)	n	$E_{0.2}$/GPa	n´	b	a	σ_u /$\sigma_{0.2}$
LF-M1	195	170	281	319	340	715	0.34	2.18	54.5	5.96	27.02	2.53	1447	315	2.55
LF-M2	199	180	292	335	359	708	0.36	2.20	56.5	6.19	21.08	2.53	1364	336	2.42
LF-M3	190	155	288	329	353	711	0.34	2.17	52.1	4.83	25.74	2.94	1443	329	2.49
AVG.	195	141	287	328	355	710	0.35	2.19	54.4	5.66	22.61	2.66	1418	327	2.48
SF-M1	184	102	343	401	445	747	0.38	2.24	47.9	2.47	50.41	2.16	1423	423	2.17
SF-M2	196	122	316	414	457	736	0.40	2.25	50.2	3.14	39.96	2.19	1330	437	2.33
SF-M3	172	98	337	398	456	720	0.41	2.24	51.6	2.42	49.48	2.06	1266	436	2.13
AVG.	184	107	332	430	453	734	0.39	2.24	49.9	2.68	53.62	2.13	1340	432	2.21
CF-M1	205	160	261	307	345	668	0.33	2.18	42.9	6.12	19.31	1.59	1478	320	2.55
CF-M2	189	178	259	307	343	659	0.33	2.19	46.6	7.98	14.93	1.52	1385	321	2.54
CF-M3	186	165	262	310	347	698	0.34	2.18	50.1	6.47	18.24	1.67	1446	322	2.66
AVG.	193	167	261	308	345	675	0.33	2.18	46.5	6.87	17.49	1.59	1437	321	2.58

Note: E is the Young's modulus; $\varepsilon_{0.2}$ and $\varepsilon_{2.0}$ are the strain value of offset strain of 0.2% and 2.0%; ε_u is the ultimate strain. $\sigma_{0.01}$, $\sigma_{0.2}$, $\sigma_{1.0}$, and $\sigma_{2.0}$ are the stress values corresponding to offset strains of 0.01%, 0.2%, 1%, and 2%.

The stress-strain curves of stainless steel under the monotonic tensile loading are presented in Fig. 5. Unlike carbon steel, it can be seen that 1) stainless steel exhibits nonlinear stress-strain behavior without a yield plateau and well-defined yield point; the stress corresponding to the offset strain 0.2% was usually used as the nominal yield stress; 2) it requires a more complex and suitable monotonic model than the bilinear model usually used in steel. Three commonly used nonlinear metal constitute modes [28-30], given by Eq. (1) to Eq. (3), were adopted to describe the stress-strain curves with the fitted constitute parameters obtained from the experimental tests listed in Table 3.

I) Ramberg-Osgood Model

$$\varepsilon = \frac{\sigma}{E} + 0.002\left(\frac{\sigma}{\sigma_{0.2}}\right)^{n} \tag{1}$$

II) G-N Model

$$\varepsilon = \begin{cases} \dfrac{\sigma}{E} + 0.002\left(\dfrac{\sigma}{\sigma_{0.2}}\right)^{n} & \sigma \le \sigma_{0.2} \\ \dfrac{\sigma-\sigma_{0.2}}{E_{0.2}} + \left(0.008 - \dfrac{\sigma_{1.0}-\sigma_{0.2}}{E_{0.2}}\right)\left(\dfrac{\sigma-\sigma_{0.2}}{\sigma_{1.0}-\sigma_{0.2}}\right)^{n_{0.2,1.0}} + \varepsilon_{t0.2} & \sigma_{2.0} < \sigma \end{cases} \tag{2}$$

III) Quach Model

$$\varepsilon=\begin{cases}\dfrac{\sigma}{E}+0.002\left(\dfrac{\sigma}{\sigma_{0.2}}\right)^{n} & \sigma\le\sigma_{0.2}\\ \dfrac{\sigma-\sigma_{0.2}}{E_{0.2}}+\left(0.008-\dfrac{\sigma_{1.0}-\sigma_{0.2}}{E_{0.2}}\right)\left(\dfrac{\sigma-\sigma_{0.2}}{\sigma_{1.0}-\sigma_{0.2}}\right)^{n'_{0.2,1.0}}+\varepsilon_{t0.2} & \sigma_{0.2}<\sigma\le\sigma_{2.0}\\ \dfrac{\sigma-a}{b+\sigma} & \sigma>\sigma_{2.0}\end{cases} \quad (3)$$

where E and $E_{0.2}$ are the Young's modulus and the corresponding elastic modulus when the offset strain is 0.2%. n and $n'_{0.2,1.0}$ are the coefficients of strain hardening; $\sigma_{0.2}$ and $\sigma_{1.0}$, are the stress values which correspond to offset strains of 0.2% and 1%, respectively; and a and b are parameters in the R-O constitutive model. A more detailed explanation of the monotonic tensile constitutive model is referred to in [31, 32].

A comparison between the fitting curves and the testing curves is shown in Fig. 5. It can be concluded that the Ramberg-Osgood model with a single constitutive parameter accurately represents the stress-strain curve until the strain is below 0.2%; however, it would overestimate the strain hardening degree of stainless steel with the strain increases. Both the G-N and Quach models can fit the stress-strain curve exactly while the strain is over 0.2% and less than 2.0%. However, it is not recommended to use the G-N model to represent the stainless steel in the case of large strains due to significant deviation, e.g., the strain is larger than about 5.0%. In general, the Quach model is the most accurate monotonic tensile constitutive model for stainless steel with complicated parameters and is recommended for describing the monotonic tensile stress-strain curve in cases with large strain.

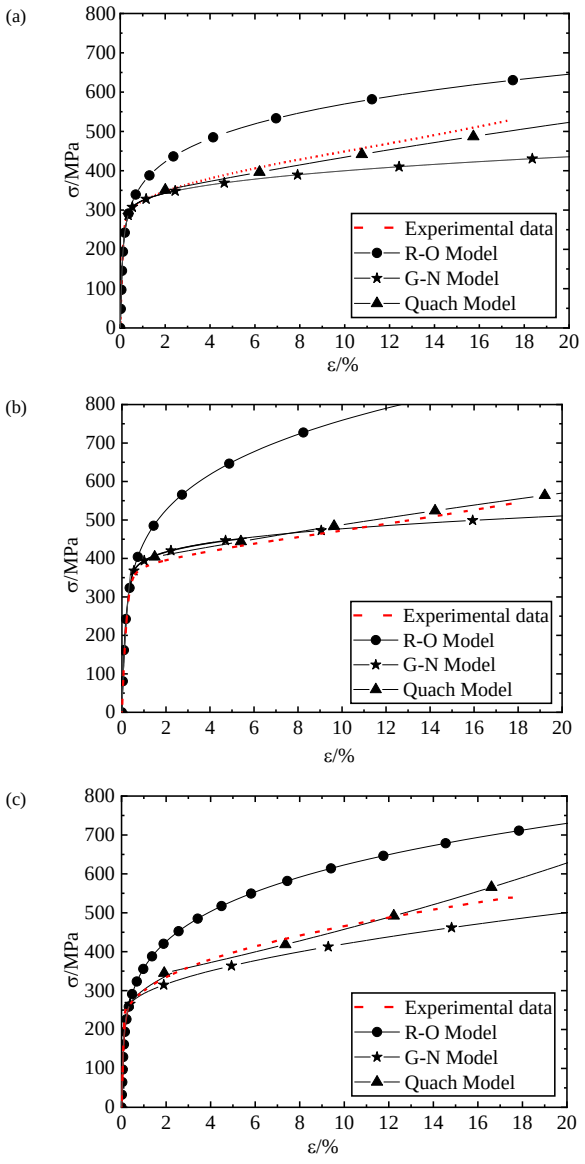

Fig. 5 Monotonic tensile σ-ε curve: (a) LF; (b) SF; and (c) CF

3.2. Results of cyclic loading experiments

In this section, the stress-strain curves of the specimens under completely reversed constant strain amplitude in the cyclic loading are illustrated and analyzed. The parameters of cyclic hardening are calibrated; the strain-fatigue life relationship is established. First, it is essential to discuss the effect of the buckling-restrained device and the notch on the test data before the analysis of the stress-strain relationship.

When the specimens were compressed under cyclic loading, the cross section along the thickness of the LF specimen enlarged, and friction force was generated between coupons and the buckling-restrained device. Further, the lateral deformation of specimens caused by the Poisson effect was restrained on account of the buckling-restrained device. As a result, the measured axial force is the summation of the compressive stress, friction force, and lateral force. In order to understand the influence of friction and lateral force on the axial compress, comparisons between stress-strain curves with and without the buckling-restrained device are plotted and shown in Fig. 6. It can be concluded that the difference between the two curves is negligible, and the stress values are approximately the same under identical strain. Therefore, the compressive stress in the present paper is directly measured by the axial stress without considering the influence of friction and the Poisson effect.

The stress-strain curves of coupons with and without the notch were shown in Fig. 7 to show the influence of the notch on the specimens' performance. The notch has little effect on the mechanical properties in the case of small strain or little number hysteresis, but it has a great impact on the specimens' strain-fatigue life, which will be introduced in detail in Chapter 3.2.3. The stainless steel's cycle characteristics in this section are analyzed with LF specimens.

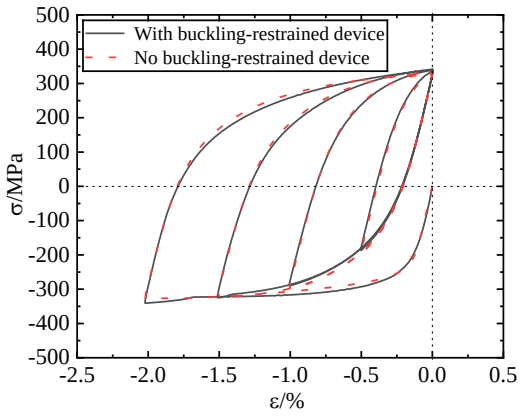

Fig. 6 Effect of buckling-restrained device on stress

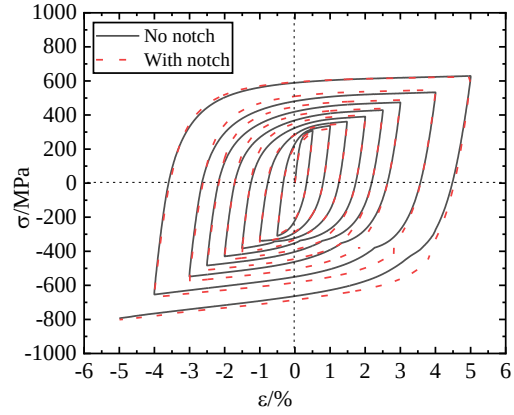

Fig. 7 Effect of the notch on stress

3.2.1. Skeleton curve

To analyze the characteristics of the stress-strain response under various strain amplitudes and to compare its difference with the monotonic tensile curve, a family of stable hysteresis loops which corresponds to the half fatigue life under each constant strain amplitude was plotted in a similar graph. The cyclic skeleton curve was generally fitted using the Ramberg-Osgood model [33], which is given in Eq. (4) by tracing the peak stress tips of each hysteresis curve (shown in Fig. 8).

$$\frac{\Delta\varepsilon}{2}=\frac{\Delta\varepsilon_e}{2}+\frac{\Delta\varepsilon_p}{2}=\frac{\Delta\sigma}{2E}+\left(\frac{\Delta\sigma}{2K'}\right)^{1/n'} \quad (4)$$

where $\Delta\varepsilon$, $\Delta\varepsilon_e$, and $\Delta\varepsilon_p$ are the total, elastic, and plastic amplitudes; $\Delta\sigma$ is the total stress amplitude; E is the Young's modulus; K' is the coefficient of cyclic strength; and n' is the exponent of cyclic strain hardening that can be fitted by the peak stress versus strain amplitude data by ordinary least squares.

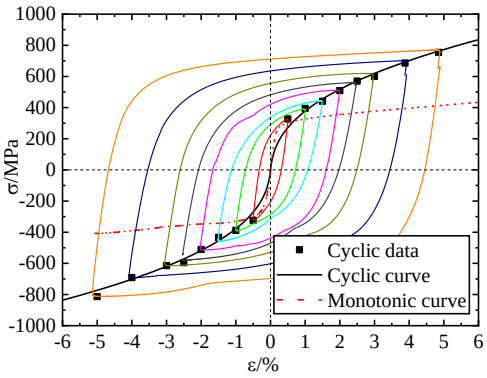

Fig. 8 Constant strain amplitude cyclic skeleton curve

It can be seen that the hysteresis curves of stainless steel are shuttle-shaped with good symmetry and plump, indicating good hysteretic performance as well as energy dissipation. The hysteresis curve width gradually increases with the increment of the strain amplitude, indicating that the share of plastic strain amplitude rises. The cyclic skeleton curve of stainless steel, observed from the above-mentioned figure, is always over the monotonic tensile curve, showing evident cyclic hardening. With the augmentation of the strain amplitude, the difference between the cyclic loading curve and monotonic tensile curve continues to grow, indicating a more obvious strain hardening. The stress under cyclic loading at the 5% strain is approximately 1.63 times the stress of the monotonic tensile loading. Therefore, it is inappropriate to apply the monotonic tensile curve of stainless steel to calculate the hysteretic behavior in elastoplastic studies, as the monotonic tensile curve would underestimate the strain hardening characteristic under cyclic tension-compression loading. The fitted cyclic skeleton curve does not accurately pass through all stress tips, the reason is that the cyclic plastic parameters were calibrated by the average value of tensile and compressive stress but are not equal to each other due to the kinematic hardening during cyclic loading.

From the test results, the calculated values of cyclic hardening parameters K' and n' under different loading cases, including constant and variable strain amplitudes were listed in Table 4. The cyclic hardening parameters fitted under various strain amplitudes were different from each other, indicating that the cyclic skeleton curve is greatly affected by strain amplitude and loading history. These cyclic hardening parameters between loading case L11 and L12 represent a small difference under the loading system with the same strain amplitude but opposite loading order. Loading cases L13 and L14 have the same phenomenon. The results reveal that the hysteretic characteristics of the stainless steel are less affected by the direction of tension and compression, and the buckling-restrained device restrained the buckling effect of the specimen under compression well.

Table 4
Cyclic loading skeleton curve parameters

Case	L1-L10	L11	L12	L13	L14	AVG.
K′/MPa	2213	1376	1375	1806	1956	1745
n′	0.428	0.405	0.413	0.468	0.519	0.447

Comparisons of the cyclic skeleton and monotonic tensile curves under several typical cyclic loading systems with different amplitudes are shown in Fig. 9. When the Ramberg-Osgood model is used to fit the cyclic skeleton curves, some results are acceptable under partial strain amplitudes, but the deviation is larger in some strain amplitudes. For example, in the small strain amplitude (the strain is less than 1.5% in Fig. 9 (a) and (b)) and a few initial loading laps (the first two loops at 4% and 5% in Fig. 9 (c) and (d)). The reason for this may be related to the cumulative plastic strain value, but further research is needed to verify this conclusion. Fig. 9 (c) and (d) show that the peak stress value of the first large strain at ±5% under variable strain amplitude loading cases L13 and L14 coincides with the stress versus large strain of monotonic tensile curve, confirming accuracy of the test.

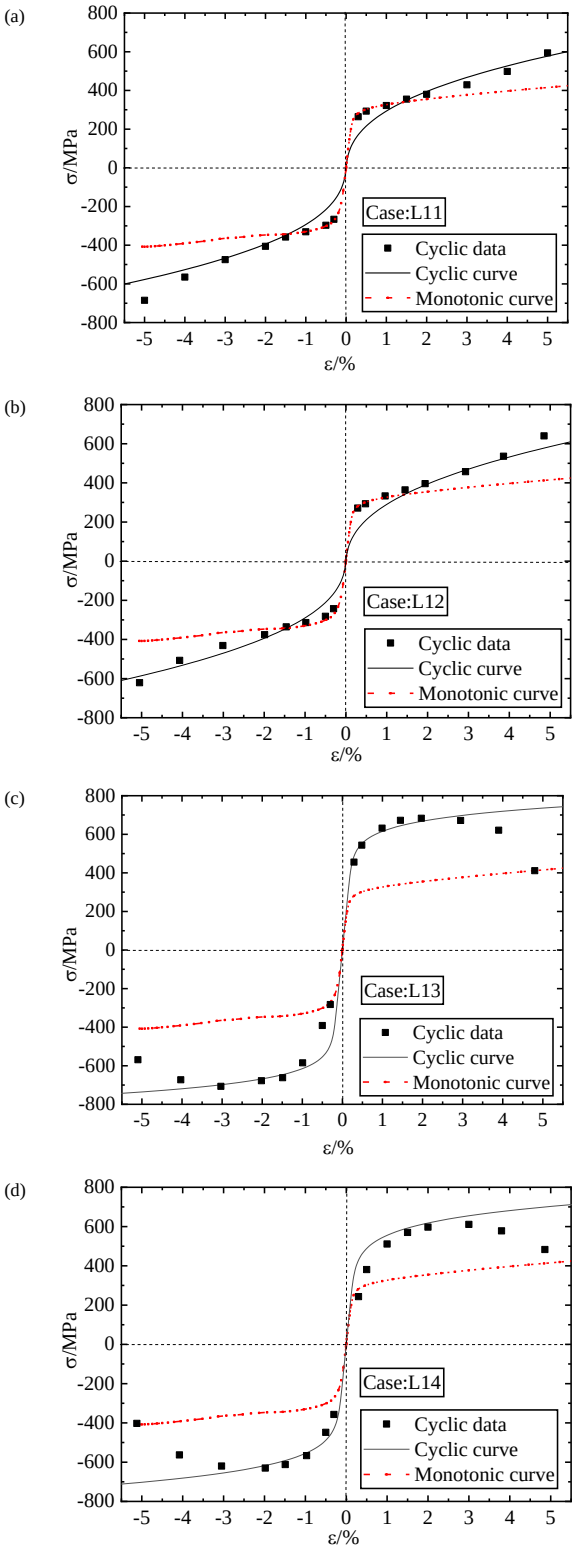

Fig. 9 Variable strain amplitude cyclic skeleton curve

3.2.2. Cycle stress-strain characteristics

The changes in the stress-strain hysteresis loop along with the increasing number of fatigue cycles (N_f) under fully reversed constant strain amplitudes are shown in Fig. 10. In terms of each given strain amplitude, the hysteresis curves do not overlap and exhibit cyclic hardening or softening as the cumulative plastic strain increases. Fig. 11 shows the stress amplitude variation against the increasing number of fatigue cycles (N_f) under each constant strain value and also explains the trend of cyclic behavior in another aspect.

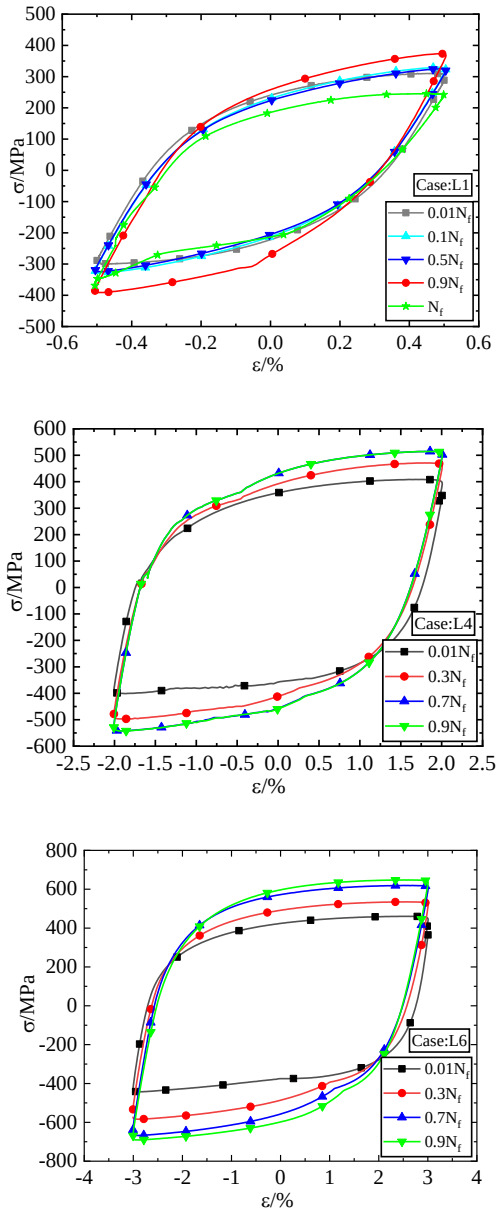

Fig. 10 Change of the hysteresis loop with an increasing number of fatigue cycles (N_f) under constant amplitude strain

The characteristics of cyclic behavior for stainless steel can be summarized from the above-mentioned figure: 1) The specimens have obvious cyclic softening before fracturing along with an increase of cumulative plastic damage if the total strain is less than 1%. The specimens have undergone four stages; slight hardening also occurred at first several cycles. And then, it came into being relatively stable for a long duration. Then, slight cyclic softening occurred before the second phase of significant cyclic hardening until fracture with a rapid drop of stress. This phenomenon is consistent with the findings in [34]. 2) When the total strain is between 1% and 2%, the specimens have undergone three stages: a greater cyclic hardening during the initial stage compared with the case where the strain is less than 1%, followed by cyclic stabilizing for a short period, then a second cyclic hardening appeared before fracture; there is no cyclic softening in the whole process. 3) In the case with a strain amplitude over 2%, the maximum cyclic stress increases until the specimen fractures, and no cyclic stabilizing and softening were observed. The specimen only undergoes one stage with cyclic hardening until fracture. It is a continuous-growth process in the peak stress where the rate grew slowly along with the number increment of fatigue cycles in the later stage.

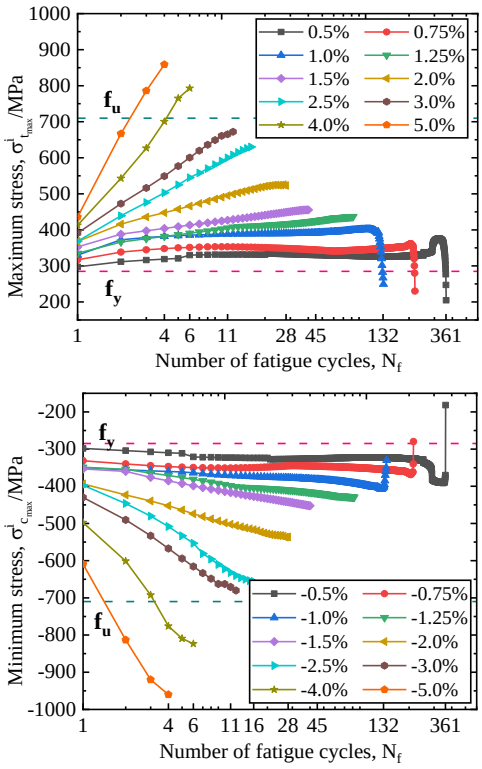

Fig. 11 Change of the peak stress with the increasing number of fatigue cycles (N_f) of LF specimen under constant strain amplitude loading: (a)Tensile stress; (b) Compressive stress

The peak value of cyclic tensile and compressive stress changes in sync with the increasing number of fatigue cycles (N_f). The cyclic stress peak exceeded the ultimate stress only when the value of strain is larger than 4%. And the peak cyclic stress remained between the yield stress and the ultimate stress if the strain amplitude is less than 4%. This phenomenon is different from the discovery in [7], which reported that the peak cyclic stress exceeds the ultimate stress after approximately thirteen load reversals at a strain amplitude of 2%.

To quantify the cyclic hardening magnitude, a measure is defined in Eq. (5), which employs the ratio of the maximum cyclic stress $\sigma_{t,\max}^{N=N_f}$ during the whole life to the stress amplitude $\sigma_{t,\max}^{N=1}$ at the first cycle corresponding to the same strain. It is also an important indicator in seismic design:

$$R = \frac{\sigma_{t,\max}^{N=N_f} - \sigma_{t,\max}^{N=1}}{\sigma_{t,\max}^{N=1}} \tag{5}$$

The cyclic hardening ratios increase gradually along with the increments of strain amplitude under fully reversed strain-control, as illustrated in Table 5. It can be fitted into a straight line roughly with a slope of 0.22 that is passing through the origin point, as shown in Fig. 12, indicating that stainless steel S30408's cyclic hardening degree increases linearly with the increase in strain amplitude.

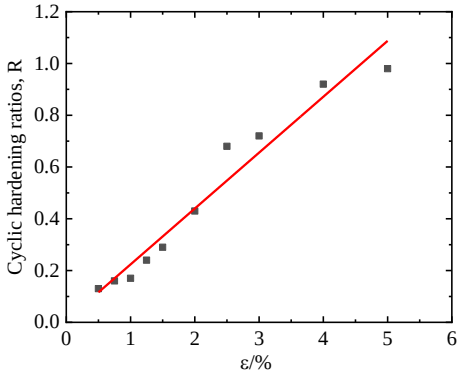

Fig. 12 The cyclic hardening ratios under different constant strain amplitude

The stiffness of the material decreases quickly after yielding when plain carbon steel is used as the core component of BRB, resulting in a large residual displacement [35, 36]. The significant cyclic hardening of stainless steel with strong post-yield stiffness can alleviate the core of BRB from generating large offset strain during cyclic loading for energy dissipation components, which can increase the safety margin of the structure.

Table 5
Degree of cyclic hardening of LF specimen

Case	L1	L2	L3	L4	L5	L6	L7	L8	L9	L10
$\sigma_{t,\max}^{N=1}$ / MPa	297	316	332	347	352	368	374	391	412	435
$\sigma_{t,\max}^{N=N_f}$ / MPa	334	369	390	431	455	525	630	672	792	858
R*	0.13	0.16	0.17	0.24	0.29	0.43	0.68	0.72	0.92	0.98

*Note: R is the ratio of the peak stress increment in the cyclic loading process to the maximum stress in the first cycle.

3.2.3. LCF life

The LCF life of specimens subjected to cyclic loading is also an important factor to be considered in the seismic structure application. The strain-fatigue life relationship is employed through the constant strain amplitude test results, which vary from 0.5% to 5.0%.

The total strain-fatigue life relationship contains two parts: the elastic part corresponding to the description of the Basquin model [37, 38]; and the plastic part, which corresponds to the description of the Manson-Coffin model [39-41]. The curves of the elastic and plastic strain vs the fatigue life (ε-2N_f) are linear on the diagram with log-log coordinates. This paper employs the Basquin-Manson-Coffin model described in Eq. (6), which takes elasticity and plasticity into account to fit the strain-fatigue life relationship of Austenitic stainless steel S30408 in all specifications mentioned above.

$$\frac{\Delta\varepsilon}{2}=\frac{\sigma_f^{'}}{E}\left(2N_f\right)^b+\varepsilon_f^{'}\left(2N_f\right)^c \tag{6}$$

where Δε is the total strain amplitude, σ′$_f$ and ε′$_f$ are the coefficients of fatigue strength and fatigue ductility, *b* and *c* are the exponents of fatigue strength and fatigue ductility, and 2N_f represents the number of reversals to failure.

The parameters shown in Table 7 were derived using the mean of the specimens' fatigue life shown in Table 6 under each strain amplitude. The plots illustrating the number of reversals against elastic, plastic, and total strain amplitudes with logarithmic coordinates are presented in Fig. 13. Then, the relative cumulative plastic deformation strain value (CPD_{rv}) [42], which is an important indicator used to measure the capacity of energy dissipation, was calculated through Eq. (7), in which ε_{pi} is the plastic strain range of the *i*th cycle, ε_y is the nominal yield strain:

$$CPD_{rv}=\Sigma\left|\Delta\varepsilon_{pi}\right|/\varepsilon_y \tag{7}$$

The results concluded that the fatigue life of stainless steel S30408 decreases gradually along with the increment of the strain amplitude, as shown in Table 6. The cumulative plastic deformation capacity and ductility also gradually decrease, which is shown by the decreasing value of CPD_{rv}, on account of the increasing plastic damage. The plastic strain, which accounts for the majority of the total strain, has a great influence on the material's low-cycle fatigue life, seen in Fig. 13; further, the Basquin-Manson-Coffin model can fit the materials' strain-fatigue life, because there is good agreement between the fitted curve (described in Eq. (6) with fatigue parameters) and the test data.

Table 6
Results of the low-cycle fatigue life

Δε/2(%)	Δε$_p$/2(%)	2N$_f$				LF′/LF	CPDrv/(LF′)			
		LF	SF	CF	LF′		LF	SF	CF	LF′
0.5	0.325	722	532	560	5024	6.95	1564	1152	1213	10855
0.75	0.535	426	365	306	2342	5.49	1221	1046	877	9293
1.0	0.735	264	204	182	1036	3.92	1108	856	764	4351
1.25	1.015	162	115	133	726	3.42	996	707	818	4466
1.5	1.26	90	62	60	474	5.27	687	473	458	3619
2.0	1.67	56	-	46	256	4.57	561	-	461	2567
2.5	2.13	32	-	20	-	-	408	-	255	-
3.0	2.58	22	-	-	-	-	325	-	-	-
4.0	3.51	12	-	-	-	-	238	-	-	-
5.0	4.45	8	-	-	-	-	204	-	-	-

Table 7
Parameters of Basquin-Manson-Coffin model

Specimen	LF	SF	CF	LF′
σ$_f$′	1108	769	819	1738
b	-0.1848	-0.1195	-0.1300	-0.1789
ε$_f$′	0.1369	0.1133	0.1006	0.3307
c	-0.5246	-0.5241	-0.4902	-0.5358

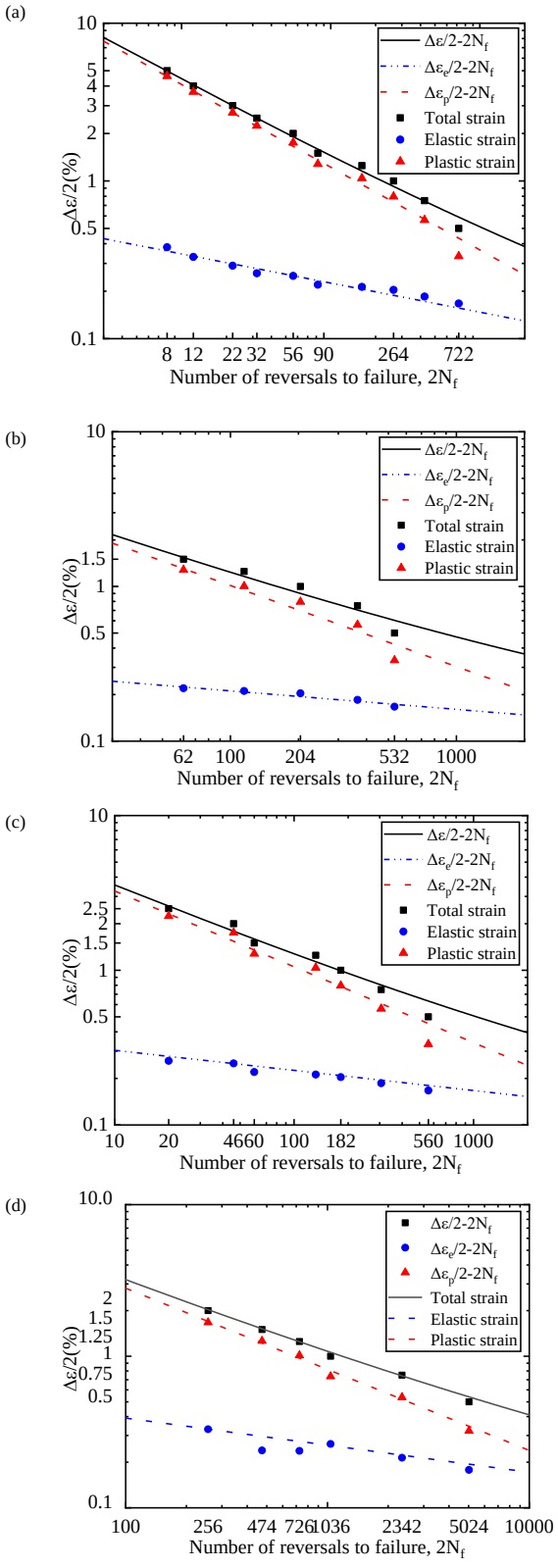

Fig. 13 Strain-fatigue life relationship: (a) LF; (b) SF; (c) CF; (d) LF´

Fig. 14 plots the test data for the number of reversals versus the constant strain for all specifications and their Basquin-Manson-Coffin curves with a total strain amplitude of 5%. By comparing the strain-fatigue life relationship of different specification specimens LF, SF, and CF, it can be summarized that the material's fatigue life is less affected by the specimen size. The hysteresis cycle number corresponding to the specimens with different sizes they can withstand is not much different. Comparing the fatigue life of specimen LF with a notch and specimen LF' without a notch in the same specification characters shows that the maximum ratio of the number of hysteresis cycles for LF' to LF can be up to about seven times at the same strain amplitude, which proves that the notch has a significant influence on the low-cycle fatigue performance, and even small damage would reduce the fatigue life of the material significantly.

Fig. 15 illustrates the comparison of strain-fatigue life curves between the test results of LF specimens and that in previous literature[7,12,13]. The results show that there exists a great difference among the fitted fatigue life curves of Austenitic stainless steel S30408 obtained by each paper, which may be related to the production batch of the material and the test process of the specimen. However, this needs further study and confirmation. It is obvious from Fig. 15 that the variation trend of fatigue life with the strain amplitude increase of Austenitic stainless steel S30408 in this test is close to that in reference [13], but the experimental fatigue life is much lower. The test result for this experiment is between the strain-fatigue life curve fitted in references [7] and [12], which proves that the deviation of the test results is not large and is reasonable. In this cyclic loading test, the peak strain value of the LF specimen reached ±5%. There are more data values and a larger strain range compared with the fitted stain-fatigue curves in the previous literature (<2%) [7,12,13]. Although the initial damage caused by the notch on the LF specimen will lead to a reduction of fatigue life, it is reliable and relatively conservative to use the fitted strain-fatigue life equation of the LF specimen to predict the fatigue cycles of Austenitic stainless steel S30408 as less than the strain amplitude of 5%. The damage is inevitable due to the cutting and welding factors in the processing of material and components, and the fatigue life is sensitive to damage under large strain loading.

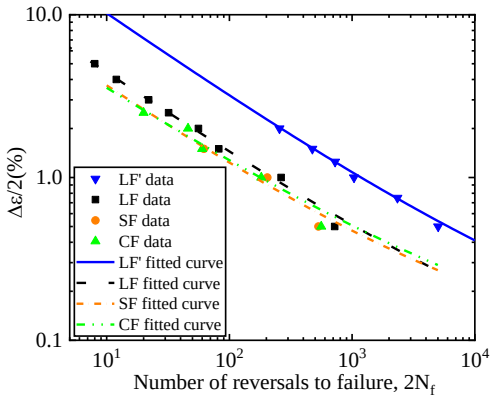

Fig. 14 Comparison of strain-fatigue life curve for different specimens

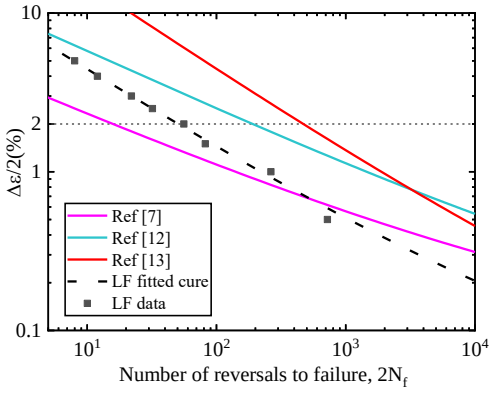

Fig. 15 Comparison of the strain-fatigue life between the test results of the LF specimen and other literature

4. Finite element modeling

The experimental results in the previous section show the basic properties of Austenitic stainless steel S30408 under axial tensile loading and the stress-strain characteristics under cyclic loading, which are useful for understanding how the material works. And it is necessary to further study the specific hardening paremeters of the material under cyclic loading for representing the hysteretic behavior accurately in finite element analysis. In addition, a numerical simulation of the structures and components under reciprocating loading is needed in the absence of tests. The precise material cyclic plasticity parameters are beneficial for the response analysis of structures. In this section, the behavior of specimens is analyzed and simulated using finite element software under variable strain amplitude cyclic loading to further understand hysteretic performance and provide basic data for the seismic analysis of stainless steel structures.

4.1. Calibration of mixed hardening parameters

It is concluded from the cyclic stress-strain relationship curve that the austenitic stainless steel S30408 exhibits a nonlinear mixed hardening behavior, which includes isotropic hardening and kinematic hardening under cyclic loading. That means the evolution rule of the subsequent yield surface includes two parts: 1) an isotropic hardening process that depicts the yield surface expansion through equivalent strain; and 2) a kinematic hardening process that describes the yield surface translation in the stress space via backstress.

The nonlinear mixed hardening model is numerically built-in Abaqus [43], which employs the Chaboche constitutive model put forward by Armstrong and Frederick [44-46] and improved by Chaboche [14]. This model can be used to describe characteristics of the material under cyclic loading, such as nonlinear strain hardening, the Bauschinger effect, the ratcheting effect, and mean stress relaxation. The cyclic plastic model parameters are calibrated, and the test and simulation curves are compared.

According to the von Mises yield criterion, the strengthening expression is calculated as follows:

$$F = f(\sigma - \alpha) - \sigma^0 = 0 \tag{8}$$

where σ denotes the tensor of stress, α represents the backstress tensor, and σ^0 refers to the current yield stress, indicating the size of the yield surface.

The plastic flow law of the model associated with von Mises yield criterion is as follows:

$$\dot{\varepsilon}^{pl} = \dot{\bar{\varepsilon}}^{pl} \frac{\partial F}{\partial \sigma} \tag{9}$$

The evolution in the yield surface size, as defined by the isotropic hardening component, is a function of the equivalent plastic strain, which is calculated by:

$$\sigma^0 = \sigma|_0 + Q_\infty \left(1 - e^{-b\varepsilon^p}\right) \tag{10}$$

where $\sigma|_0$ denotes the yield stress when the plastic strain is zero, which can be obtained from the first-quarter cycle of the test, Q_∞ and b are the model's isotropic hardening parameters, and ε^p is the equivalent plastic strain.

The determination of the elastic limit stress is dependent on the detection accuracy of the offset strain because the stainless steel has no yield platform and exhibits an obvious nonlinear stress-strain relationship. It is appropriate to use 0.55 times the nominal yield stress at a 0.2% offset strain as the yield stress $\sigma|_0$. And there gave a detailed introduction to the definition of the elastic limit stress in references [47, 48]. Q_∞ denotes the maximum change value of the yield surface size, indicating the hardening degree, and b denotes the rate of the yield surface size changes with the equivalent increase in the plastic strain.

The size of the yield surface stress σ_i^0 in the ith cycle is calculated from the average of the peak tensile stress σ_i^t and the maximum elastic limit compressive stress σ_i^c:

$$\sigma_i^0 = \frac{\sigma_i^t - \sigma_i^c}{2} \tag{11}$$

The equivalent plastic strain which corresponds to the yield surface σ_i^0 is:

$$\varepsilon_i^p = 2\Sigma\left(\Delta\varepsilon_{i-1}^p\right) + \frac{1}{2}\Delta\varepsilon_i^p \tag{12}$$

where $\Delta\varepsilon_i^p$ is the range of plastic strains corresponding to the ith cycle. The equivalent plastic strain equals the sum of twice of the plastic strain range of the (i-1)th cycle and half of the plastic strain of the ith cycle.

The isotropic hardening model formula described in Eq. (10) has been fitted by data pair (σ_i^0, ε_i^p), including the data ($\sigma|_0$,0) when the equivalent plastic strain is zero, and then hardening parameters Q_∞ and b are obtained.

To better depict the kinematic hardening under high plastic strain, multiple sets of backstress were selected, which are expressed as:

$$\alpha_k = \frac{c_k}{\gamma_k}\left(1 - e^{-\gamma_k \varepsilon^p}\right) + \alpha_{k,1} e^{-\gamma_k \varepsilon^p} \tag{13}$$

$$\alpha_{NLK} = \sum_{k=1}^{N} \alpha_k \tag{14}$$

where α_k is the backstress, C_k represents the kinematic hardening modulus in the initial stage, and γ_k represents the rate of change in the kinematic hardening modulus, along with the plastic deformation. k is the Chaboche component number.

The plastic strain corresponding to the backstress is shifted as follows:

$$\varepsilon_j^p = \varepsilon_j - \frac{\sigma}{E} - \varepsilon_p^0 \tag{15}$$

where $\varepsilon_1^p = 0$, and ε_p^0 is the value of plastic strains at the time the hysteresis loop passes through the X axis. The backstress α_j is calculated by:

$$\alpha_j = \sigma_j - \sigma_s \tag{16}$$

where $\sigma^s = (\sigma_1 + \sigma_n)/2$ is the mean value of the first data point σ_1 and last data point σ_n, representing the size of the stable yield surface. Data pairs (α_j, ε_j^p) are used to fit the model described in Eqs. (13) and (14) to calculate kinematic hardening parameters c_k and γ_k.

From general experience with stainless steel, the application of two to five backstress components may obtain a better fitting result. The stress-strain curve shows that the backstress curve contains several distinct shape features: 1) an initial part close to a straight line; 2) a curve segment with a sharp curvature; 3) a curve segment with a smaller curvature; and 4) a straight part close to flat to the end. Therefore, the number of backstresses is N=4, which corresponds to the count of the characteristic for the kinematic hardening curve. In order to prevent over-fitting while fitting the kinematic hardening parameters C and γ, it is necessary to calibrate parameters manually at first by using the endpoints of each curve segment [47]. More detailed steps are referred to in the literature [49, 50]. The final fitted results were obtained and are presented in Table 8.

Table 8
Fitted parameters of Chaboche constitutive model

Parameters	Q_∞	b	C_1	γ_1	C_2	γ_4	C_3	γ_4	C_4	γ_4
First fitted	177	7.5	13183	174	9497	83	4112	36	1271	20
Optimize	284	5	15894	432	9050	154	4359	52	1422	20

4.2. Comparison between test and simulation curves

The ABAQUS was utilized to simulate the cyclic loading test. Regarding the specimens' symmetry, half of the specimen size was simulated by using solid element C3D8R, and the material properties values were obtained based on the monotonic tensile test and the previous calibration of cyclic hardening parameters in section 4.1. The end of the specimen clamped by the actuator hydraulic jaws was applied fixed constraint in the simulation. The reference point and the loading surface were set for coupling constraint to have the same deformation, and the set displacement amplitudes were applied to the reference point. The FEM and specimen details are shown in Fig. 16.

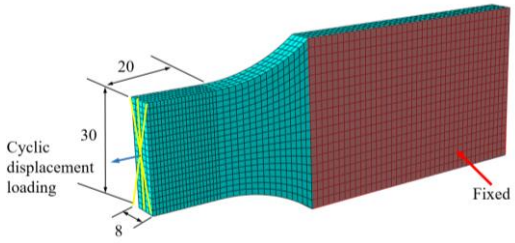

Fig. 16 FEM and specimen details

The experiments and simulation curves were carried out for comparison under the various strain amplitude cyclic loadings. Fig. 17 shows that the mixed hardening parameters obtained by fitting can depict the key behavior characteristic of the hysteresis curves and can be applied to simulate the test curve acceptably. In addition, the parameters can provide a data basis for seismic analysis of the stainless steel structure.

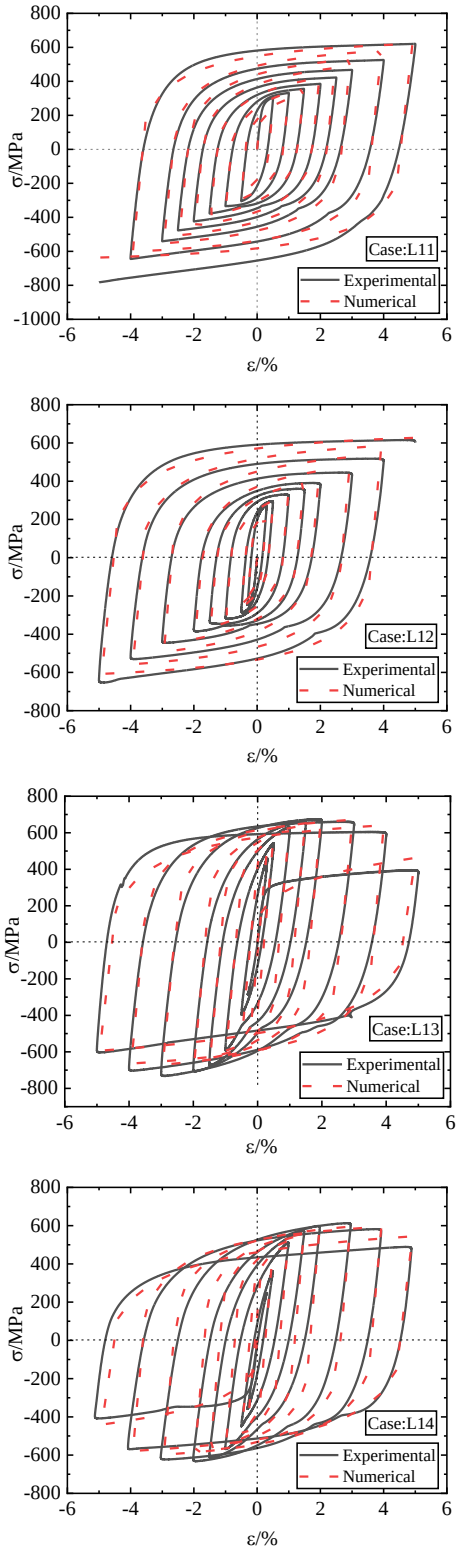

Fig. 17 Comparison of the σ-ε curve under variable strain amplitude between the test and simulation

5. Conclusion

This study analyzed the basic mechanical properties under the monotonic tensile loads, and the characteristics of the hysteretic loop under cyclic loads with a larger strain amplitude (5%) of Austenitic stainless steel S30408. We calibrated the cyclic plastic parameters, and the strain-fatigue life relationship was obtained based on the constant strain amplitude varying from 0.5% to 5.0%. Furthermore, variable strain amplitude loading tests were performed to calibrate the mixed hardening model parameters for application in numerical simulations. The above-presented investigation was summarized below.

(1) The stress-strain of Austenitic stainless steel S30408 shows nonlinear characteristics without a yield plateau, presenting a large strength yield ratio of about 2.5 and high strain hardening that indicates a higher safety redundancy in seismic design. The Quach model fits the monotonic tensile curve well.

(2) The hysteresis curve of Austenitic stainless steel S30408 is shuttle-shaped with good symmetry and plumpness with constant strain amplitude, which reveals good hysteretic behavior and energy dissipation. Cyclic hardening was observed in that the cyclic skeleton curve is above the tensile skeleton curve. The Ramberg-Osgood model employed to fit the cyclic skeleton curve was appropriate, whose hardening parameters were calibrated.

(3) The cyclic stress of the material varies along with increasing the number of reversals, which consists of cyclic hardening, cyclic softening, and cyclic stability phenomena. The cyclic hardening ratio is the peak stress throughout the whole fatigue life to the maximum stress of the first cycle versus the same strain amplitude to indicate the cyclic hardening degree. The larger the strain value, the higher the cyclic hardening degree.

(4) The fatigue life is mainly affected by plastic strain, and it declines slowly with the augment of the strain amplitude. The Basquin-Manson-Coffin model fits the strain-fatigue life well, and the calibrated fatigue parameters could predict the low-cycle fatigue life of Austenitic stainless steel S30408 in a larger plastic strain range (5%).

(5) The Chaboche constitutive model employed in Abaqus, representing a mixed hardening model comprising isotropic and kinematic hardening, can simulate the performance of Austenitic stainless steel S30408 by comparing the test data under variable strain amplitude cyclic loading.

Declaration of competing interest

The authors declare that they have no known competing financial interests or personal relationships that could have appeared to influence the work reported in this paper.

Acknowledgments

The work was financially supported by the National Natural Science Foundation of China (No. 51778206), which is gratefully acknowledged.

References

[1] L. Gardner, The use of stainless steel in structures, Progress in Structural Engineering & Materials 7(2) (2005) 45-55.
[2] A. Pramanik, A.K. Basak, Stainless steel: Microstructure, mechanical properties and methods of application (2015).
[3] Q. Jing, X. Fang, Application of Stainless Steel Reinforcements in the Hong Kong-Zhuhai-Macao Bridge, 2016 International Conference on Architectural Engineering and Civil Engineering 72 (2017) 363-366.
[4] G.P. Cimellaro, S. Marasco, Capacity Design, 2018.
[5] S. Avgerinou, I. Vayas, High-strength steel on dissipative elements in seismic resistant systems: Tests and simulations, Journal of Constructional Steel Research 172 (2020) 106173.
[6] I. Arrayago, E. Real, L. Gardner, Description of stress-strain curves for stainless steel alloys, Materials & Design 87(DEC.15) (2015) 540-552.
[7] C.-D. Annan, E. Beaumont, Low-cycle fatigue of stainless steel plates under large plastic strain demands, Journal of Building Engineering 29 (2020).
[8] F. Zhou, L. Li, Experimental study on hysteretic behavior of structural stainless steels under cyclic loading, Journal of Constructional Steel Research 122 (2016) 94-109.
[9] X. Chang, L. Yang, L. Zong, M.H. Zhao, F. Yin, Study on cyclic constitutive model and ultra low cycle fracture prediction model of duplex stainless steel, Journal of Constructional Steel Research 152(JAN.) (2019) 105-116.
[10] A. Belattar, C. Keller, L. Taleb, Multiscale analysis of the pre-hardening effect on the cyclic behavior and fatigue life of 304L stainless steel, Mat Sci Eng a-Struct 662 (2016) 468-480.
[11] H. Ban, J. Zhu, G. Shi, Cyclic loading tests on welded connections of stainless-clad bimetallic steel and modelling, Journal of Constructional Steel Research 171 (2020) 106140.
[12] Julie, Colin, Ali, Fatemi, Said, Taheri, Fatigue Behavior of Stainless Steel 304L Including Strain Hardening, Prestraining, and Mean Stress Effects, Journal of Engineering Materials & Technology 132(2) (2010) 021008-1-13.
[13] J. Colin, A. Fatemi, S. Taheri, Cyclic hardening and fatigue behavior of stainless steel 304L, J Mater Sci 46(1) (2011) 145-154.
[14] J.L. Chaboche, Time-independent constitutive theories for cyclic plasticity, International Journal of Plasticity 2(2) (1986) 149-188.
[15] A. Kumar, S. Vishnuvardhan, G. Raghava, Evaluation of Combined Hardening Parameters for Type 304LN Stainless Steel Under Strain-Controlled Cyclic Loading, Transactions of the Indian Institute of Metals 69(2) (2016) 513-517.
[16] N. Moslemi, M.G. Zardian, A. Ayob, N. Redzuan, S. Rhee, Evaluation of Sensitivity and Calibration of the Chaboche Kinematic Hardening Model Parameters for Numerical Ratcheting Simulation, Applied sciences9(12) (2019) 2578.
[17] SG. Fan, RM. Ding, YL. Han, Experimental study on bearing capacity of austenitic stainless steel lipped channel columns [j]. Advanced Steel Construction, 2020, 16(1): 65-76.
[18] SG. Jia, QH. Tan, JY. Ye, Experiments on dynamic mechanical properties of austenitic stainless steel S30408 and S31608 [J]. Journal of Constructional Steel Research, 179 (2021) 106556.

[19] J. Lanning, G. Benzoni, C.M. Uang, Using Buckling-Restrained Braces on Long-Span Bridges. I: Full-Scale Testing and Design Implications, Journal of Bridge Engineering 21(5) (2016) 04016001.
[20] Uang, Chia-Ming, Benzoni, Gianmario, Lanning, Joel, Using Buckling-Restrained Braces on Long-Span Bridges. II: Feasibility and Development of a Near-Fault Loading Protocol, Journal of Bridge Engineering (2016).
[21] R.A. Chacon, M.D. de Marco, E. Real, I. Arrayago, An experimental study on the cyclic response of austenitic stainless steel, in: Proceedings of the 9th International Conference n Advances in Steel Structures; ICASS 5–7, 2018. December 2018,Hong Kong, China
[22] P. Dusicka, A.M. Itani, I.G. Buckle, Cyclic response of plate steels under large inelastic strains, Journal of Constructional Steel Research 63(2) (2007) 156-164.
[23] C.n. standard, G.T. 228.1-2010, MaterialsTensile Testing-Part 1: Method of Test at Room Temperature 2010.
[24] R Ge, Y Xu, X Niu, Experimental study on low-cycle fatigue behavior of Chinese LYP225, China Civil Engineering Journal (1) (2017) 12-19. (in Chinese)
[25] C.n. standard, G.T. 26077-2010, Metallic materials-Fatigues testing-Axial-strain-controlled method 2010.
[26] K.H. Nip, L. Gardner, A.Y. Elghazouli, Cyclic testing and numerical modelling of carbon steel and stainless steel tubular bracing members, Steel Construction 32(2) (2010) 424-441.
[27] K.H. Nip, L. Gardner, C.M. Davies, A.Y. Elghazouli, Extremely low cycle fatigue tests on structural carbon steel and stainless steel, Journal of Constructional Steel Research 66(1) (2010) 96-110.
[28] SEI/ASCE 8-02, Specification for the Design of Cold-Formed Stainless Steel Structural Members, New York: American Society of Civil Engineers (ASCE), 2002.
[29] L Gardner, D A Nethercot. Experiments on stainless steel hollow sections-Part 1: Material and cross-sectional behavior, Journal of Constructional Steel Research, 2004, 60(9): 1291－1318.
[30] W M Quach, J G Teng, K F Chung. Three-Stage Full-Range Stress-Strain Model for Stainless Steels, Journal of Structural Engineering, 2008, 134(9):1518–1527.
[31] I. Arrayago, E. Real, L. Gardner, Description of stress-strain curves for stainless steel alloys, Materials & Design 87 (2015) 540-552.
[32] D Fernando, J G Teng, W M Quach, et al. Full-range stress-strain model for stainless steel alloys, Journal of Constructional Steel Research, 2020, 173:106266.
[33] W. Ramberg, W.R. Osgood Description of Stress-Strain Curves by Three Parameters Technical Note No.902, WashingtonDC: National Advisory Committee for Aeronautics, 1943.
[34] J.W. Pegues, S. Shao, N. Shamsaei, J.A. Schneider, R.D. Moser, Cyclic strain rate effect on martensitic transformation and fatigue behaviour of an austenitic stainless steel, Fatigue & Fracture of Engineering Materials & Structures (2017).
[35] R Tremblay, P Bolduc, Neville, R.D. , Seismic testing and performance of buckling-restrained bracing systems, Canadian Journal of Civil Engineering 33(2) (2006) 183-198.
[36] C.J. Black, N. Makris, I.D. Aiken, Component Testing, Seismic Evaluation and Characterization of Buckling-Restrained Braces, Journal of Structural Engineering 130(6) (2004) p.880-894.
[37] O. BASQUIN, The exponential law of endurance tests, Proc ASTM 10 (1910).
[38] A Kulesa, A Kurek, T Agoda, et al. Low Cycle Fatigue of Steel in Strain Controlled Cyclic Bending, Acta Mechanica et Automatica, 2016, 10(1).
[39] Manson, Behavior of Materials Under Conditions of Thermal Stress, Nat. Advis. Comm. Aero. Tech 2933 (1953).
[40] C. Jr, A study of the effects of cyclic thermal stresses on a ductile metal, A Study of the Effects of Cyclic Thermal Stresses on A Ductile Metal (1953) 931-950.
[41] Z Zheng, G Cai, Z Li, et al. Interpretation of Manson-Coffin Model of Low Cycle Fatigue Based on Damage Mechanics[J]. China Mechanical Engineering, 2011, 22(7):812-814.
[42] B Huang, Q Chen, T Li. Low-cycle fatigue test of Q235 steel buckling-restrained braces, China Civil Engineering Journal, 2013,46 (6): 29-43(in Chinese)
[43] D.C.S. Simulia, Abaqus 6.11 analysis user's manual, Abaqus 6.11 Documentation (2011) 22-22.
[44] R. Milligan, W. Koo, T. Davidson, The Bauschinger Effect in a High-Strength Steel, Journal of Basic Engineering 88 (1965) 34.
[45] P.J. Armstrong, C.O. Frederick, A mathematical representation of the multiaxial Bauschinger effect. CEGB Report RD/B/N 731, Central Electricity Generating Board. the report is reproduced as a paper: 2007, Materials at High Temperatures 24(1) (1966) 1-26.
[46] Y. Jiang, P. Kurath, Characteristics of the Armstrong-Frederick type plasticity models, International Journal of Plasticity 12(3) (1996) 387-415.
[47] A. Kalnins, J. Rudolph, A. Willuweit, Using the Nonlinear Kinematic Hardening Material Model of Chaboche for Elastic-Plastic Ratcheting Analysis, Journal of Pressure Vessel Technology 137 (2015) V01BT01A005.
[48] ASME, Boiler and Pressure Vessel Code, American Society of Mechanical Engineers, New York, 2010.
[49] T. Gilman, B. Weitze, J. Rudolph, A. Willuweit, A. Kalnins, Using Nonlinear Kinematic Hardening Material Models for Elastic-Plastic Ratcheting Analysis, ASME 2015 Pressure Vessels and Piping Conference, 2015.
[50] W.F. Weitze, T.D. Gilman, Additional Guidance for Inelastic Ratcheting Analysis Using the Chaboche Model, American Society of Mechanical Engineers, Pressure Vessels and Piping Division (Publication) PVP 1 (2014).